

Density Matrix Emulation of Quantum Recurrent Neural Networks for Multivariate Time Series Prediction

J.D. Viqueira,^{1,2,*} D. Faílde,¹ M. M. Juane,¹ A. Gómez,¹ and D. Mera²

¹*Centro de Supercomputación de Galicia (CESGA), 15705 Santiago de Compostela, Spain*
²*Computer Graphics and Data Engineering (COGRADE), Departamento de Electrónica e Computación, Universidade de Santiago de Compostela, 15782 Santiago de Compostela, Spain*
(Dated: November 1, 2023)

Quantum Recurrent Neural Networks (QRNNs) are robust candidates to model and predict future values in multivariate time series. However, the effective implementation of some QRNN models is limited by the need of mid-circuit measurements. Those increase the requirements for quantum hardware, which in the current NISQ era does not allow reliable computations. Emulation arises as the main near-term alternative to explore the potential of QRNNs, but existing quantum emulators are not dedicated to circuits with multiple intermediate measurements. In this context, we design a specific emulation method that relies on density matrix formalism. The mathematical development is explicitly provided as a compact formulation by using tensor notation. It allows us to show how the present and past information from a time series is transmitted through the circuit, and how to reduce the computational cost in every time step of the emulated network. In addition, we derive the analytical gradient and the Hessian of the network outputs with respect to its trainable parameters, with an eye on gradient-based training and noisy outputs that would appear when using real quantum processors. We finally test the presented methods using a novel hardware-efficient ansatz and three diverse datasets that include univariate and multivariate time series. Our results show how QRNNs can make accurate predictions of future values by capturing non-trivial patterns of input series with different complexities.

I. INTRODUCTION

Processing and analysing multivariate time series, generally involve sophisticated algorithms that load high-dimensional datasets evolving in time, wherein temporal correlations are not trivial. In classical computation, Machine Learning is a consolidated approach for prediction and anomaly detection tasks [1–7]. Recurrent Neural Networks (RNNs) are a powerful tool for learning sequential data [8], and, over decades, several variations over the first model have improved their performance, like the well-known *Long Short-Term Memory* (LSTM) or the *Gated Recurrent Unit* (GRU) cells [1, 4, 9]. Transformers are a recent alternative [10] that seems to outperform the previous Neural Network models. However, there is not enough experience when using this algorithm for numerical multivariate time series.

The RNN models feature great results for sequential learning, but they are not problem-free. Some models cannot store information from first inputs in long time series. The LSTM cell arose to address this problem [1]. Moreover, because of the temporal correlations between different variables in multivariate time series, a high-dimensional space appears for computing data with non-linear patterns. Thus, it is necessary to build neural networks with more neurons, layers and parameters, which are computationally expensive and more challenging to train. Rapidly, we have to tackle a Deep Learning task, which requires computational resources and algorithms that ease the parameter optimisation during the

neural network training, such as the backpropagation algorithm for estimating the gradients [11].

Quantum Machine Learning (QML) leverages the power of Quantum Computing to produce complex patterns that are probably not straightforwardly reproducible in a classical computer [12, 13]. However, in the current *Noisy Intermediate-Scale Quantum* (NISQ) era of quantum computers, there is a need for algorithms requiring a low quantum circuit depth, since only a limited number of operations are meaningful. Consequently, a substantial part of the research in quantum algorithms is focusing on the Variational Quantum Algorithms (VQAs) [14]. A VQA lies on hybrid classical-quantum routines to classically minimise a cost function computed with a back-end Parameterised Quantum Circuit (PQC).

In this context, a VQA can be used as a Neural Network by feeding a quantum circuit with information from our dataset and then tuning the circuit parameters to minimise the cost function [15]. The first proposals of Quantum Recurrent Neural Networks (QRNNs) consist of a temporal loop that feeds a quantum state into a quantum circuit and applies the Schrödinger equation to evolve the state. Their applications were simulating stochastic processes [16] and stochastic filtering of signals with noise [17, 18]. In the middle of the NISQ era and with the explosion of Machine Learning, several proposals have arisen to enhance the power of the current Machine Learning models by adding Parameterised Quantum Circuits as part of the algorithm [19–23].

The actual QRNN model seeks to maximise the use and the power of Quantum Computing by a PQC that computes the whole sequence, and the only classical part

* josedaniel.viqueira@rai.usc.es

is data pre-processing, data post-processing and the optimisation of circuit parameters [24–29]. The most common circuit architecture repeatedly encodes classical data into the quantum circuit, applies a unitary operator and measures a subset of qubits, involving multiple intermediate measurements before the end of the circuit. However, other proposals avoid intermediate measurements at the expense of increasing the number of qubits with the time-series length [27] or truncating the circuit [29].

The QRNN model is expected to provide advantages compared to classical neural networks, which extend to QML models in general. The encoding of classical data into quantum states allows us to compute a number of functions that increases exponentially with the number of qubits [15]. This feature enhances non-linearities that are required for learning complex patterns. In classical computing, the process requires exponential resources. Besides that, circuits with intermediate measurements, known as dynamic circuits, are not widespread in the QML literature, but they can lead to a new realm of algorithms on real quantum hardware [30], and they are being introduced in Quantum Computing platforms [31, 32].

The main aim of this article is to provide the mathematical tools to emulate this type of circuit, which is the core of QRNN algorithms. This is very interesting for two reasons: with the mathematical formulation, we can learn about the propagation of information through the quantum circuit, and the emulation makes the algorithm compatible with classical devices, before sending it to a quantum computer. Within this context, we test the theoretical procedure in several use cases, showing their potential for multivariate time series prediction.

The manuscript is structured as follows. In Section II we provide the method for emulating a quantum circuit with intermediate measurements, which has the property of returning values that depend on past data encoded in the circuit, like recurrent neural networks. As backpropagation is used in classical Machine Learning, in Section III we provide a method to analytically compute first- and second-order partial derivatives of the circuit outputs, by an expansion of the Parameter Shift Rule (PSR) [15, 33]. In Section IV we show the results after applying the former methods to an emulation of a QRNN for multivariate time series prediction, in order to demonstrate that the algorithm works by emulating the quantum circuit with the presented method. Finally, discussions are included in Section V.

II. FORMULATION OF THE QRNN STATES WITH DENSITY MATRICES

The QRNN model is based on the classical RNN model, as proposed by [25]. Following this approach, we explicitly provide a tensor representation of the internal states propagated through the QRNN and its outputs, based on the density matrix formalism. This represen-

tation allows the implementation of a classical emulator based on tensor operations and even simple matrix operations, which are very fast in current computational devices.

A. The classical Recurrent Neural Network

Consider a set of data which is time-ordered,

$$\{\mathbf{x}_{(0)}, \mathbf{x}_{(1)}, \dots, \mathbf{x}_{(t)}, \dots, \mathbf{x}_{(T)}\}, \quad (1)$$

that is the input multivariate time series, since each item is a vector containing the information of n_v variables. The output series is

$$\{\mathbf{y}_{(0)}, \mathbf{y}_{(1)}, \dots, \mathbf{y}_{(t)}, \dots, \mathbf{y}_{(T)}\}, \quad (2)$$

which is the target in the Machine Learning task.

The output of a RNN at time t depends on the inputs from the previous time steps since it preserves past information with a form of memory [34]. The easiest way to imagine a network with memory is thinking in a box that continuously receives and returns data. To start, the box is supplied with an input, $\mathbf{x}_{(0)}$, and it returns two objects: an output $\bar{\mathbf{y}}_{(0)}$ which is read, and a *hidden state* $\mathbf{h}_{(0)}$ which is re-introduced in the box next time. From the second time onwards, the box receives the previous hidden state $\mathbf{h}_{(t-1)}$ and the input $\mathbf{x}_{(t)}$. Then, it computes them and generates the output $\bar{\mathbf{y}}_{(t)}$ and the hidden state $\mathbf{h}_{(t)}$ to be re-introduced. The model is represented in Fig. 1, where we can see the recurrence, so that the behaviour is dynamic, in contrast to feedforward neural networks, for which the information is never transmitted backwards.

The information flux in a RNN through time splits into three different lines, represented in Fig. 1, that stand for *input data* $\mathbf{x}_{(t)}$, *output data* $\bar{\mathbf{y}}_{(t)}$ and *hidden state* $\mathbf{h}_{(t)}$. Both $\bar{\mathbf{y}}_{(t)}$ and $\mathbf{h}_{(t)}$ are functions that depend on $\mathbf{x}_{(t)}$ and $\mathbf{h}_{(t-1)}$,

$$\begin{cases} \bar{\mathbf{y}}_{(t)} = \mathcal{Y}(\mathbf{x}_{(t)}, \mathbf{h}_{(t-1)}) \\ \mathbf{h}_{(t)} = \mathcal{S}(\mathbf{x}_{(t)}, \mathbf{h}_{(t-1)}) \end{cases}, \quad (3)$$

but at the same time, $\mathbf{h}_{(t-1)}$ also depends on previous inputs and a hidden state. Functions \mathcal{Y} and \mathcal{S} are the part which is expensive to compute. They consist of matrix calculations that take into account the tunable parameters (weights), structure and connections between the layers of neurons that form the network.

B. The Quantum Recurrent Neural Network

The QRNN leverages the power of PQCs implicitly performing matrix calculus. Like in the proposed classical model, wherein a network returns output data every time step, we measure the quantum circuit to obtain data

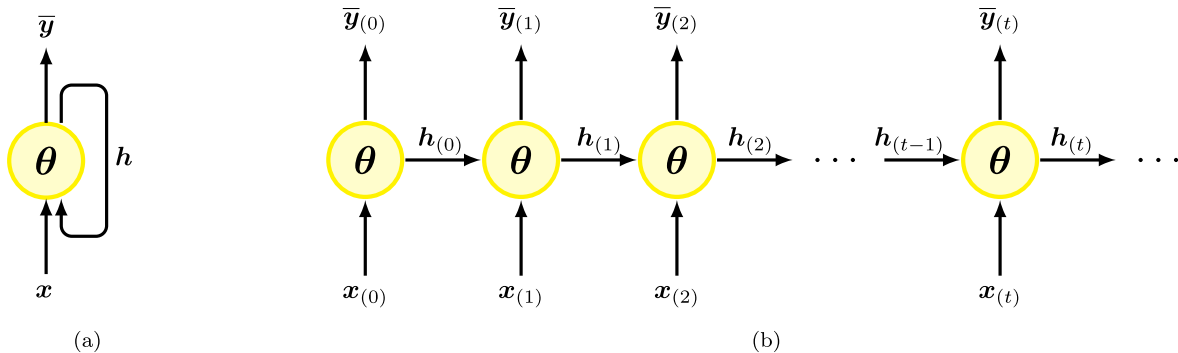


FIG. 1. Classical Recurrent Neural Network representations. (a) Basic RNN scheme. (b) Basic RNN unrolled through time.

in our classical devices. Quantum Networks also contain a *hidden-state* flux \mathbf{h} . As its name suggests, a hidden state propagates internally and carries information not required to be known. That is why we can think of a quantum state as a hidden state. This quantum state is actually a mixed state that arises from the measurement of a subsystem A, and a subsystem B, which is not measured, provided that A and B are entangled.

Hence, we can now construct a general circuit that resembles the classical RNN described above, as it was proposed by [25]. Since a quantum circuit diagram represents the series of operations applied over several qubits (vertical direction) during the time (horizontal direction), the circuit in Fig. 2 can be interpreted as the unrolled representation through time of the QRNN. The circuit consists of two quantum registers: an *exchange register* (E) with n_E qubits, and a *memory register* (M) with n_M qubits. The former is used to exchange information between the quantum and the classical interface, by applying encoding and measurement operations, while the latter is never measured. The total number of qubits is n . We then have a circuit *block* for every time step: an estimation of an output from the input at time t . The instructions are (see Fig. 2):

1. Initialise register E (M) to a desired pure state $|\Psi_E\rangle$ ($|\Psi_M\rangle$). We will restrict the initialisation of all the qubits to $|0\rangle$.
2. Reset of register E. All register E qubits start at $|0\rangle$ every time step.
3. Apply a parameterised unitary (ansatz) $U(\mathbf{x}_t, \boldsymbol{\theta})$ that evolves the state of each qubit and entangles some (or all) qubits from both registers E and M, correlating the information from both. $\boldsymbol{\theta}$ are the variable parameters (weights) of the network.
4. Measure qubits from register E.
5. Repeat steps (2), (3), and (4) iteratively from $t = 1$ to $t = T$.

The unitary $U(\mathbf{x}_t, \boldsymbol{\theta})$ must encode the classical input \mathbf{x}_t each time step, apply parameterised gates depending

on the set of weights $\boldsymbol{\theta}$, and apply entanglement between registers E and M. The $\boldsymbol{\theta}$ are always the same for the different repetitions of the unitary, following the classical approach (see Fig. 1).

Variations of this structure are available in the literature [28] when trying to create a circuit that sustains the coherence for a longer time. This is not the scope of this work, since we want to establish some bases for designing and emulating quantum RNNs. Solutions for NISQ-era limitations in these networks will require further research that may involve quantum hardware parameters, such as the readout features or the coherence itself [35].

C. Memory and output of a QRNN

The way the vanilla RNN [36] (from which subsequent RNN algorithms were originated) operates data is the ideal sample of how data is explicitly processed in a RNN:

$$\begin{aligned} \mathbf{h}_t &= \sigma_h (W_{hx}\mathbf{x}_t + W_{hh}\mathbf{h}_{t-1} + \mathbf{b}_h), \\ \bar{\mathbf{y}}_t &= \sigma_y (W_{yh}\mathbf{h}_t + \mathbf{b}_y), \end{aligned} \quad (4)$$

being $\{W_{hx}, W_{hh}, W_{yh}\}$ matrices with the weights, $\{\mathbf{b}_h, \mathbf{b}_y\}$ the biases, and $\{\sigma_h, \sigma_y\}$ the activation functions. Matrices (2-dimension tensors) are always represented by uppercase letters, while vectors (1-dimension tensors) are represented by bold lowercase letters.

A density matrix formalism is behind the classical emulation of the quantum circuit in Fig. 2. In this case, we can compute the exact probability distribution in every measurement of n_E qubits. At the same time, we include non-unitary operations, such as the measurement itself and the reset operation. An alternative is a state-vector emulation by sampling outputs, i.e., measurement probabilities are computed from multiple circuit executions, like in a real quantum device. However, exact probabilities are preferable when emulating circuits in VQAs, especially when the optimisation method is based on gradients.

Following the instructions to build the quantum circuits, we formulate the expressions to compute two ob-

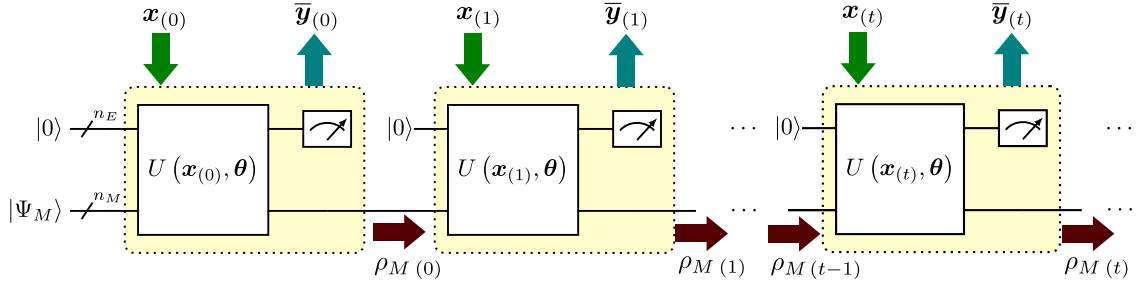


FIG. 2. General form of the QRNN circuit. Arrows show the information flux.

jects for every time step, as in Eq. (4): one is the reduced density matrix $\rho_M(t)$, which transmits information from t to $t+1$, while the other one is the expected value of some observable $\langle O \rangle_{(t)}$ (the output before classical post-processing). Following the density matrix formalism, we get

$$\begin{aligned} \rho_M(t) &= \text{Tr}_E [U \rho(t) U^\dagger], \\ \langle O \rangle_{(t)} &= \text{Tr} [U \rho(t) U^\dagger O \otimes I^{\otimes n_M}], \end{aligned} \quad (5)$$

where $\rho(t)$ is the initial density matrix of the circuit at time t after the reset on register E and before applying the operator $U = U(\mathbf{x}(t), \boldsymbol{\theta})$. O is our observable, that will be, without loss of generality, diagonal. If the observable were not diagonal, we could get its spectral decomposition and apply the necessary transformations to the circuit(s) before measurement. The output (prediction) at time t is

$$\bar{y}_{(t)} = f(\langle O \rangle_{(t)}), \quad (6)$$

being f an arbitrary function. We are restricting to a single-variable output. However, the generalisation for multiple variables is straightforward by considering a set of multiple observables instead of a single one.

This section aims to derive a tensor representation of both $\rho_M(t)$ and $\langle O \rangle_{(t)}$ to (i) provide an explicit formula that can be implemented in a classical computer as matrix products, and (ii) show how the information is transmitted through the quantum circuit.

For the derivation of the formulas, a symbol and a group of r indices (lowercase letters) represent every mathematical object that is a r -rank tensor. The ordering of the indices follows the next criteria. A subindex in parenthesis refers to the current time step, and we can sometimes neglect it. The rest of the indices identify the coefficients for every projector or vector inside the Hilbert space. Indices above (below) correspond to the base vectors in the Hilbert space (dual Hilbert space). For quantum operators over the full circuit and density matrices representing the n qubits, indices are in pairs. The first index from the pair corresponds with register E, while the second one, with register M. We use the Einstein summation convention, i.e., terms are summed when upper and lower indices are repeated. Note that

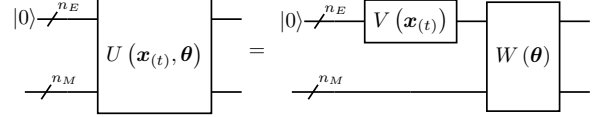


FIG. 3. Decomposition of U operator into encoding (V) and evolution part (W). The latter is the same for all the circuit blocks since $\boldsymbol{\theta}$ does not change during a circuit evaluation.

operations do not commute in general. See Appendix A for further explanation.

From now on, the dimension of the Hilbert spaces is represented by $N_E = 2^{n_E}$ and $N_M = 2^{n_M}$. The Hilbert space dimension corresponding to the $n = n_E + n_M$ qubits is $N = 2^n$.

The reduced density matrix after measurement at a time t is

$$\begin{aligned} (\rho_M)_{(t)n}^m &= U_{(t)kq}^{im} \rho_{(t)lr}^{kq} (U^\dagger)_{(t)jn}^{lr} \delta_i^j = \\ &= \sum_{i=0}^{N_E-1} U_{(t)kq}^{im} \rho_{(t)lr}^{kq} (U^\dagger)_{(t)in}^{lr}. \end{aligned} \quad (7)$$

By decomposing the operator into an encoding operator $V(\mathbf{x}(t))$ that acts only over register E and an operator $W(\boldsymbol{\theta})$ that entangles both registers (see Fig. 3), we can separate the density matrix before applying W and then have that

$$(\rho_M)_{(t)n}^m = \sum_{i=0}^{N_E-1} W_{kq}^{im} \left((\rho_E)_{(t)l}^k (\rho_M)_{(t-1)r}^q \right) (W^\dagger)_{in}^{lr}, \quad (8)$$

where $(\rho_E)_{(t)l}^k = V_{(t)0}^k (V^\dagger)_{(t)l}^0$. We have omitted (t) in W since it does not depend on time. All the blocks include the same W . We can see that $\rho_M(t)$ depends on $\rho_M(t-1)$ and $\mathbf{x}(t)$, as the hidden state in Eq. (4), unless the W operator is separable in the two registers (i.e. no entanglement between E and M).

Following Eq. (5), the expectation value of some diagonal observable $O_m^i = d^i \delta_m^i$ (no summing over i since the

symbol is above in both items) at time t is

$$\begin{aligned} \langle O \rangle_{(t)} &= (\rho_{ij}^{ikl} O_m^i \delta_n^j) \delta_{kl}^{mn} \\ &= (\rho_{ij}^{ikl} d_m^i \delta_n^j) \delta_{kl}^{mn} = (\rho_{ij}^{ikl} d_m^i \delta_n^j) \delta_{kl}^{in} \end{aligned} \quad (9)$$

where ρ' is the density matrix after applying the U operator. By decomposing this density matrix, we have

$$\langle O \rangle_{(t)} = \sum_{i=0}^{N_E-1} d^i \sum_{n=0}^{N_M-1} W_{kq}^{in} \left((\rho_E)_{(t)l}^k (\rho_M)_{(t-1)r}^q \right) (W^\dagger)_{in}^{lr}, \quad (10)$$

which, again, proves the dependency of this observable with respect to both the inputs $\mathbf{x}_{(t)}$ and the reduced density matrix from the previous step $\rho_M(t-1)$, provided that W is an operator entangling E and M. In Eq. (4), it depends on the current hidden state, not the previous one. However, the recursion makes it dependent on $\mathbf{h}_{(t-1)}$ too.

In most Quantum Machine Learning problems, the W operator is represented by a highly dense matrix (without null elements) and difficult to decompose since in general it should be formed by several entanglement layers. Then, during emulation, it is plausible to build this operator, keep it in memory and then we can split it into parts and operate with the parts as matrix products, which are very fast operations in classical computers. That splitting can be done by creating W^i matrices, which are $N_M \times N$ dense matrices. With this derivation, we do not need to compute the complete $N \times N$ density matrix before computing $\rho_M(t)$ and $\langle O \rangle_{(t)}$. Moreover, these operations are performed only once for both Eqs. (8) and (10), because the sum over n in Eq. (10) extracts the items with $m = n$ from Eq. (8). In a matrix representation, this is the trace of each of the N_E matrices that summed together give rise to $\rho_M(t)$.

III. ANALYTICAL DERIVATIVES

In Machine Learning, most parameter optimisation algorithms are based on gradients, which require some method to be computed. One is numerical differentiation, which is very inaccurate, and another one is symbolic differentiation, which is more computationally expensive [37]. Automatic Differentiation, with *backpropagation* as the most-known algorithm, seems to have many advantages.

In QML, as current circuits are prone to errors and the outputs are obtained after running the circuit multiple times (shots), systematic and stochastic errors seriously affect the estimation of the cost functions. Errors are amplified when computing numerical gradients, which makes it much more difficult to compute them unless we run circuits with a great number of shots and apply sophisticated error mitigation techniques. Automatic Differentiation as is done in classical computing

is not possible, because we need to store intermediate results through the network and intermediate quantum states cannot be accessed in real quantum devices without affecting them. To access them, we need to measure them, and they collapse.

Despite these restrictions, the Parameter Shift Rule (PSR) [15, 33] provides a method to compute analytical gradients in quantum hardware. Hereafter, we consider circuits with parameters encoded into rotation gates $R_i(\alpha) = e^{-i\alpha\sigma_i}$ generated by a Pauli matrix σ_i , because they are a set of fundamental gates used for making QMCs in gate-based quantum devices.

A. First-order partial derivatives

We define the shift expectation value at time t , $\langle O \rangle_{(t)}^{\chi} \Big|_{r_i}$, as the expectation value at time t after shifting the parameter θ_i a value χ at block $t_r < t$ in the quantum circuit. We recall that if $t_r > t$, the shift does not affect the output at time t .

For the set of gates that we consider, the shifts are $\pm \frac{\pi}{2}$ [33]. Then, in the remaining, we write only the sign.

The partial derivative of the observable at time t , $\langle O \rangle_{(t)}$, is then

$$\partial_i \langle O \rangle_{(t)} \equiv \frac{\partial \langle O \rangle_{(t)}}{\partial \theta_i} = \sum_{r=0}^t \frac{1}{2} \left(\langle O \rangle_{(t)}^+ - \langle O \rangle_{(t)}^- \right) \Big|_{r_i}, \quad (11)$$

derived in Appendix B.

In classical RNNs, the chain rule propagates backwards in time, giving rise to *backpropagation through time* (BPTT) [38]. This method is necessary for computing gradients in RNNs, as backpropagation is used in deep learning models, but it has some caveats. Firstly, it requires computing plenty of terms because we need to repeat the network the same number of time steps we have. When contributions from the beginning of the series are negligible, a possible solution is truncation methods [39]. Secondly, the propagation backwards in time requires several weights-matrix products. Instability manifests as *vanishing (exploding)* gradients if the eigenvalues of the weights matrices are lower (higher) than 1 [40]. Truncation can partially address this problem [39, 41].

From equation (11), computing the partial derivative of the observable at time t requires $2t$ function evaluations with this method. Therefore, computing the gradient requires $2tN_\theta$ function evaluations, being N_θ the number of parameters of our ansatz. The loss function for training depends on the T time steps. We can evaluate the outputs in a single circuit evaluation, i.e. running the circuit a given number of times (shots) but fixing all the parameters. Thus, in general, the number of function evaluations needed to compute the exact gradient of the loss function is $2TN_\theta$. This is worse than the case of circuits without mid-circuit measurements. Previous proposals implement techniques to reduce the number of

circuit evaluations [33, 42, 43], but not for this type of intermediate-measurement-based circuits.

Instability problems cannot appear in Quantum Neural Networks in the form of *exploding gradients* because Quantum Circuits naturally implement unitary operations [44] before measuring. Unitary operations are a restriction of some classical ML models, precisely to avoid exploding gradients, and there are ways to implement them without losing too much expressivity [45]. In the case of a QRNN, it is straightforward to see that exploding gradients cannot appear, by looking at equation (11) since the subtraction of two observables cannot blow up, and the partial derivative only involves the summation of these terms.

The *vanishing gradient* problem does appear in VQAs, where parameterised circuits can suffer from barren plateaus in the optimisation landscape [46, 47]. In the case of RNNs, vanishing gradients cause loss of memory: the network stops depending on past inputs at some moment during the training. In the QRNN model, dependencies of past inputs gradually vanish too, because, at time t , the network starts in a mixed state, $\rho_E(t) \otimes \rho_M(t-1)$, evolved by a unitary operator. The terms from $\rho_M(t-1)$ are attenuated after these operations and many circuit blocks.

B. Second-order partial derivatives

Some optimisers require the computation of the Hessian matrix, apart from the Jacobian (gradient). Some authors use the PSR to compute the Hessian [48, 49] in PQC. Here, we provide the method for computing second-order partial derivatives in the QRNN, by applying the PSR.

We define the double-shift expectation value at the time t as $\langle O \rangle_{(t)}^{\chi\lambda} \Big|_{s_j}^{r_i}$, which is the expectation value at time t after shifting the parameter θ_i in block t_r a value χ and the parameter θ_j a value λ in the block t_s of the quantum circuit.

The second-order partial derivatives are

$$\begin{aligned} \partial_i \partial_j \langle O \rangle_{(t)} &\equiv \frac{\partial^2 \langle O \rangle_{(t)}}{\partial \theta_i \partial \theta_j} \\ &= \frac{1}{4} \sum_r^t \sum_s^t \left(\langle O \rangle_{(t)}^{++} + \langle O \rangle_{(t)}^{--} \right) \Big|_{s_j}^{r_i} - \\ &\quad - \frac{1}{4} \sum_r^t \sum_s^t \left(\langle O \rangle_{(t)}^{+-} + \langle O \rangle_{(t)}^{-+} \right) \Big|_{s_j}^{r_i}, \end{aligned} \quad (12)$$

for $i \neq j$.

Moreover,

$$\begin{aligned} \partial_i^2 \langle O \rangle_{(t)} &\equiv \frac{\partial^2 \langle O \rangle_{(t)}}{\partial \theta_i^2} \\ &= \frac{1}{2} \sum_r^t \sum_s^r \left(\langle O \rangle_{(t)}^{++} + \langle O \rangle_{(t)}^{--} \right) \Big|_{s_i}^{r_i} - \\ &\quad - \frac{1}{2} \sum_r^t \sum_s^{r-1} \left(\langle O \rangle_{(t)}^{+-} + \langle O \rangle_{(t)}^{-+} \right) \Big|_{s_i}^{r_i} - \frac{1}{2} \langle O \rangle_{(t)} \end{aligned} \quad (13)$$

for $i = j$. These are derived in Appendix B.

Considering these expressions, the symmetry $\partial_i \partial_j = \partial_j \partial_i$ and that we can recycle the intermediate calculations for the final estimation of the Hessian of the loss function, the total number of function evaluations is $2T^2 N_\theta^2 + 1$ (probe in Appendix B). The symmetries allow us to reduce the computational cost. However, the scaling with time steps and number of parameters is quadratic. Some approximations would be needed to improve this scaling.

Both gradient and Hessian calculations are easy to parallelise. Then, it would be plausible to simultaneously use multiple Quantum Processing Units (QPUs) to perform several circuit evaluations. The problem is the high noise level of the current quantum hardware and different noise models for different QPUs that could complicate the optimisation process. Further investigation is required to see the scope of these architectures.

IV. RESULTS

We have implemented an algorithm that emulates a Quantum Recurrent Neural Network, by using the definitions and methods described in the previous sections. The model is based on a quantum circuit that uses a hardware-efficient ansatz. This ansatz uses layers of rotation gates for encoding classical inputs into the quantum circuit, and alternates layers of single-qubit-rotation gates parameterised by the set θ and CZ gates.

The explicit circuit ansatz $U(\mathbf{x}_{(t)}, \theta)$, used to test the performance of the general model, is represented in Fig. 4. The encoding part $V(\mathbf{x}_{(t)})$ acts only over register E qubits and repeats the encoding for each input value $R+1$ times in order to have a better expressivity [50–52]. The evolution and entanglement operator $W(\theta)$ does not vary during the circuit since it does depend always on the same parameters. We try to maximise its expressibility by repeating the entangling layers several times with different parameters.

In order to test the ideal QRNN emulation, and its learning capabilities, we use three datasets: (a) a dimmed triangular signal, (b) a non-linear damping signal with a sinusoidal perturbation, and a set (c) consisting of two non-linear damping signals as input and a linear combination of them as output. These three examples are meaningful for two reasons: the signals are nonlinear,

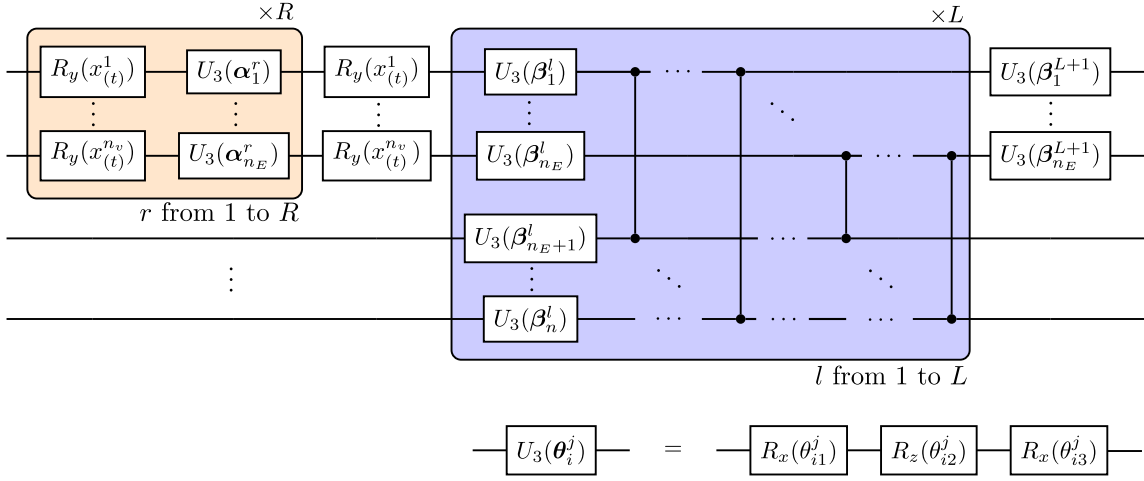


FIG. 4. QRNN ansatz, $U(\mathbf{x}_{(t)}, \boldsymbol{\theta})$, consisting of two parts. The first one is the data encoding, and gates inside the orange box are repeated with different parameters, that are a subset of trainable parameters, $\boldsymbol{\alpha}_i^r \in \{\boldsymbol{\theta}\}$. We use one qubit per input variable. The second one is the evolution and entanglement part, where the blue box is repeated L times (layers). Each layer is a column of U_3 rotations parameterised by a threesome of parameters, $\boldsymbol{\beta}_i^l \in \{\boldsymbol{\theta}\}$, and CZ gates entangling every qubit from E with every qubit from M . A final column of U_3 gates is applied over register E before measurement.

a feature that hinders the training, and are different enough to test several quantum circuit configurations. Moreover, the third one demonstrates the applicability of the model to, at least, two-variable series. Details about data generation are included in Appendix C.

The network is trained by optimising the set of parameters $\boldsymbol{\theta}$, using the L-BFGS-B algorithm [53]. We divide the series into windows of $T = 20$ points and the task is predicting 5 points for the output variable. The windows are divided into three sets: 20 % for testing, 20 % of the remaining for validation, and the rest for training. The distribution of validation samples is the same for the three datasets, but randomly generated. The loss function is the Root Mean Square Error (RMSE) between the output \bar{y} and the target series y of all the training windows. The prediction for every time step is

$$\bar{y}_{(t)} = \langle Z^{\otimes n_E} \rangle_{(t)} + b, \quad (14)$$

where Z is the σ_z Pauli matrix and b is a bias, which is an extra trainable parameter. These values are computed from an exact expectation value, without statistical variations typically arising when sampling the outputs in a real quantum computer.

The network hyperparameters used for each case are indicated in Table I. They were not optimised during this analysis, since the scope of this section is only to test the algorithm. Further works would assess different ansatz architectures, hyperparameters and optimisation techniques.

We have executed 8 different parameter optimisations for each dataset, randomly initialising the rotation gates parameters in the interval $[0, 1)$. The set of parameters after optimisation strongly depends on the initialisation. That has consequences in the training, leading to dif-

Case	n_E	n_M	L	R	N_θ
(a)	1	2	2	3	31
(b)	2	3	2	1	43
(c)	2	3	5	3	100

TABLE I. Quantum circuit configuration for each case analysed. In case (b), we re-upload input data in two qubits.

ferences in the prediction accuracy. Nonetheless, results never show a relative RMSE greater than 10 % of the series range (from -0.75 to 0.75). The set of parameters leading to the lower RMSE in the validation set are selected as the solution among the 8 different optimisation results. The corresponding datasets and their predictions are shown in Fig. 5. Table II contains the resulting RMSE of the estimated points with respect to the training, validation and test targets. The fourth RMSE corresponds to the prediction of the whole test series, not only the last 5 points of each window, by shifting the input windows 5 by 5 points.

The L-BFGS-B optimiser uses the gradient of the loss function to find its minimum. This algorithm does not compute the complete Hessian, but it makes an approximation. Then, the analytical Hessian is not needed. Furthermore, the analytical gradient can be substituted by a numerical one if the precision of the loss function is high enough. We use the default 2-point finite difference estimation with an absolute step size $\epsilon = 1 \times 10^{-8}$ implemented in the optimiser, as well as the analytical form of the gradient. For the latter, we evaluate the partial derivatives of the circuit outputs by the formulas provided in Section III, and then we apply the chain rule to calculate the gradient of the loss function.

We have compared between analytical and numerical optimisation, as shown in Fig. 6 and Table II. The op-

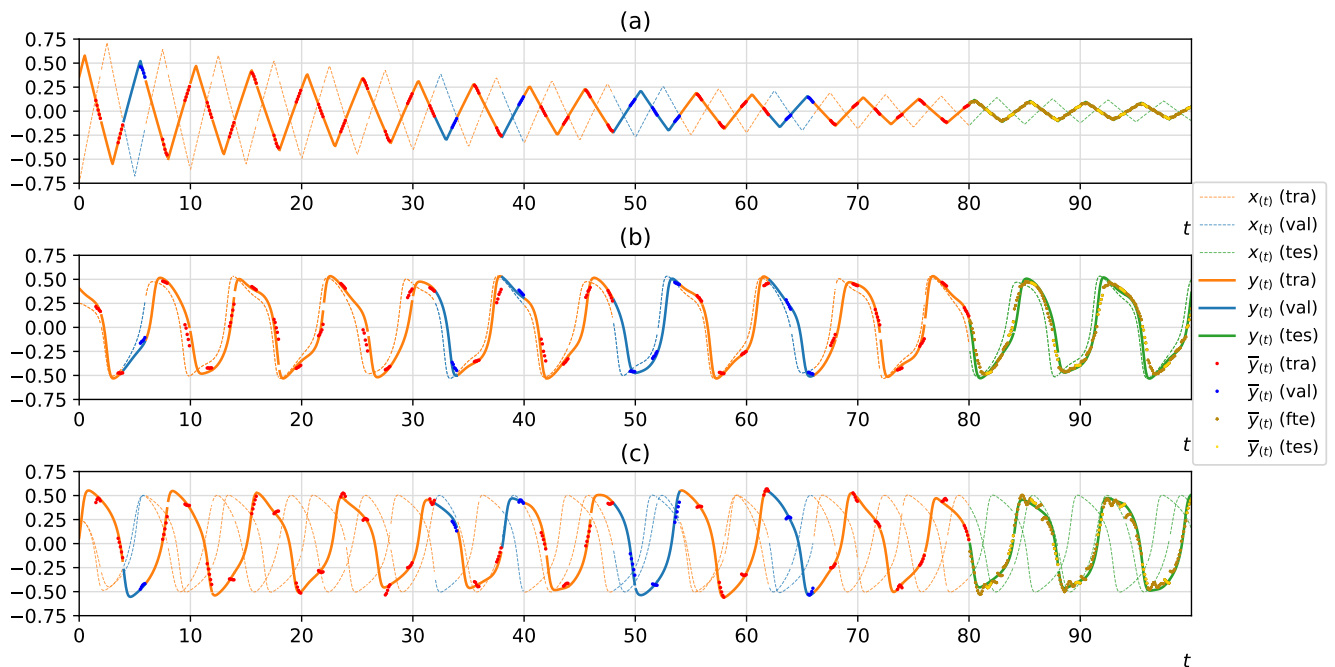


FIG. 5. Results of the learning task with each one of the three datasets. Here, numerical gradients were used. Each series was divided into windows of 20 points, each one being a sample. The neural network must predict the value of the last 5 outputs for each window, by reducing the RMSE with respect to the last 5 points of the target. Dashed lines are the inputs $\mathbf{x}(t)$, from which we make the prediction. Solid lines represent the targets. Points are the predictions. Windows are represented in orange (red), blue (dark blue) or green (dark green, pink) depending on whether the window is used for training (tra), validation (val) or testing (tes), respectively. In the test region, we add a window to make the prediction for the full test sequence (fte).

Case	Gradient	n_{it}	n_{fev}	n_{jev}	RMSE tra.	RMSE val.	RMSE tes.	RMSE fte.
(a)	analytical	600	701	701	0.006	0.011	0.004	0.005
	numerical	553	20896	653	0.005	0.008	0.003	0.004
(b)	analytical	579	664	664	0.091	0.038	0.118	0.082
	numerical	581	28556	649	0.090	0.041	0.125	0.082
(c)	analytical	1000	1082	1082	0.035	0.048	0.050	0.044
	numerical	1000	110393	1082	0.036	0.048	0.051	0.045

TABLE II. Optimisation solutions for each case with analytical and numerical gradients: number of iterations, number of function evaluations, number of Jacobian evaluations, and RMSE in training, validation and (complete) test sequences.

timisation converges to close RMSE values for both the training and validation loss curves, despite following a different trajectory in some zones. Although analytical calculations are commonly used in neural networks to improve accuracy [37], we cannot ensure that they are better in the QML tasks provided here, when emulating the circuit without any noise. Apart from that, the plots show a quick convergence in case (a), but slower in cases (b) and (c). Validation curves (and final loss values) are above the training curves in cases (a) and (c). However, they remain relatively stable and close to the training ones. Case (b) manifests validation RMSE values below the training ones, due to the distribution of validation samples. A different election would return distinct validation values. In fact, a higher number of samples should reduce the dependence on the election of validation sam-

ples. In contrast, case (c) manifests a training RMSE that slightly moves downwards from the validation one, due to a little overfitting that is not meaningful in this context. Those issues should be addressed in a complete machine learning project. Regarding they are beyond the aim of this work, we will leave them for future research.

In ideal emulation without sampling (exact), the emulated quantum circuit returns an expectation value with a precision given by the classical machine variables (e.g. float-64). As, in general, an expectation value cannot be extracted from a quantum circuit in a single shot, its evaluation by multiple repetitions (shots) of the circuit leads to stochastic variations due to this sampling process. That makes numerical gradients very inaccurate and we must use analytical gradients. The PSR allows us to tackle this problem in real quantum circuits, but

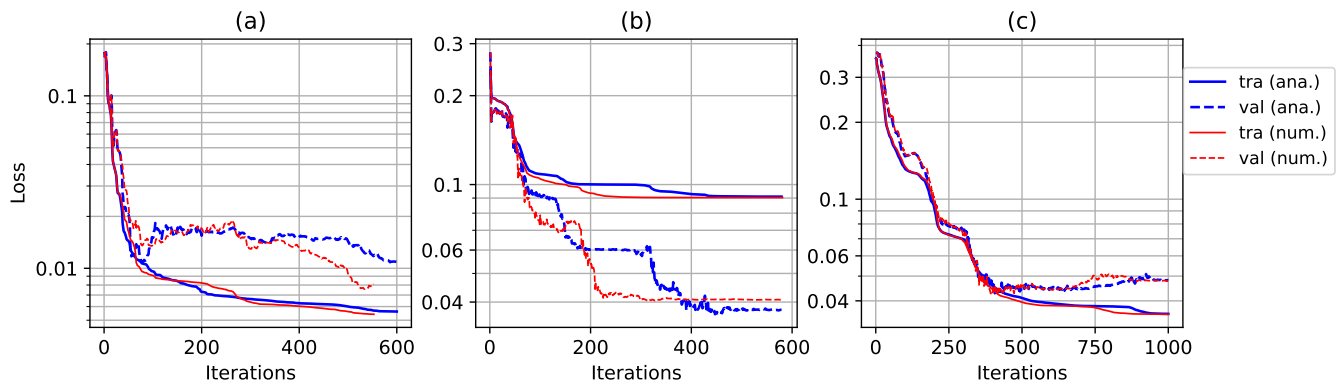


FIG. 6. Curves of optimisation for each of the three datasets, showing how the value of the RMSE varies with the iterations, for training and validation sets, and comparing results with both analytical and numerical gradients. The optimisations are those with lower final validation RMSE.

ideal exact emulation using numerical gradients requires less computational resources for the cases studied. The density matrix emulation enables exact probabilities calculation, but also simulating stochastic noise to investigate its effect on the algorithm’s performance. In the latter case, we would need analytical gradients.

The final loss values and the plots in Fig. 5 show the ability of the network to model non-trivial patterns in univariate and multivariate input series. The univariate output series estimations approximate to the output targets under a reasonable error because the RMSE is, in the worst case, an order of magnitude lower than the range of output values (from -0.75 to 0.75). The lowest error corresponds with the univariate triangular signal, because it is the simplest case. Note that, in this case, the test RMSE is lower because the series decreases in amplitude with time. Meanwhile, the errors for the damped oscillator signals increase to upper values, but the network can reliably extrapolate the time series to the test region, for both the 1-variable and 2-variable cases. Apart from that, the iterations that the optimiser needs during the training are comparable. Furthermore, the more complex, the more parameters are needed, so that qubits and layers are added with increasing complexity from the case (a) to (c). In short, our results confirm the actual applicability of QRNN models to univariate and multivariate time series prediction and their emulation through the density matrix formalism.

V. DISCUSSION

We have used the density matrix formalism to derive the formulation of the hidden states and the outputs in a Quantum Recurrent Neural Network with intermediate measurements, and its first- and second-order partial derivatives with respect to its trainable parameters. With the density matrix formulation, it is possible to directly perform an ideal emulation of the param-

eterised quantum circuit that makes up the network and we showed the results for a machine learning task with three different datasets. The analytical gradients will permit to train networks with noisy outputs coming from quantum circuits.

The QRNN was presented in previous works [24–29]. Some of them delve into the inner structure of such quantum circuits, but there was not an explicit formulation to see how quantum states are operated through the quantum circuit. With our work, we contribute to a better understanding of how information is processed inside the network, and we compare it with the classical RNN. Moreover, the given formulas allow a direct implementation of a code for emulation.

The formulation provides various remarkable advantages related to other possible methods. First of all, it avoids computing the complete density matrix of the n -qubits quantum state, whose number of elements scales as $\mathcal{O}(4^n)$, by splitting the ansatz quantum operator. Moreover, the network outputs are directly computed from the terms that build up the reduced density matrix. Secondly, density matrix formulation allows the computation of exact expectation values in circuits with intermediate measurements, which is not feasible with state-vector emulation for real cases of interest.

Consequently, the gradients can be computed with high precision in a classical computer. We have seen that parameter optimisations with numerical and analytical gradients converge to close values. The great difference between both methods is the computational cost. Analytical forms require $2T$ circuit evaluations for a gradient component, being T the number of time steps (circuit blocks inside a single circuit). Meanwhile, a 2-point finite difference approximation simultaneously shifts the parameter in all circuit blocks, needing only 2 circuit evaluations per gradient component. Nonetheless, as the precision of the variables is lost, analytical forms become necessary. Then, we expect that they will be unavoidable in emulations with noise and executions in real quantum computers. Our formulation lets us use numerical gra-

dients due to its high precision, at least for the datasets that were studied. Future work may explore the effect of quantum circuit noise. Similar conclusions apply to the Hessian calculation, which requires a T^2 factor of circuit evaluations to be computed analytically, but it is usually approximated due to its high computational cost in most cases.

In this context, the idea of distributed quantum computing, where several Quantum Processing Units work simultaneously, gathers strength. Despite the number of circuit evaluations needed, the QRNN model shows a significant feature: it does not require a lot of qubits. For the hardware-efficient ansatz and the datasets we studied, an ideal quantum processor of 5 qubits would be enough to run the circuits.

The results are promising for potential use in real cases. To this end, the model hyperparameters optimisation to enhance the power of the neural network, the adaptability to the quantum hardware limitations, research on circuit structures that capture correlations behind complex datasets and the adaptability of different optimisation techniques are starting points towards a generalised application of Quantum Recurrent Neural Networks to multivariate time series prediction.

ACKNOWLEDGMENTS

We thank the CESGA Quantum Computing group members for their feedback and the stimulating intellec-

tual environment they provide. We thank Constantino Rodríguez Ramos, especially for theoretical insights. This work was supported by Axencia Galega de Innovación through the Grant Agreement “Despregamento dunha infraestrutura baseada en tecnoloxías cuánticas da información que permita impulsar a I+D+I en Galicia” within the program FEDER Galicia 2014-2020. A. Gómez was supported by MICIN through the European Union NextGenerationEU recovery plan (PRTR-C17.I1), and by the Galician Regional Government through the “Planes Complementarios de I+D+I con las Comunidades Autónomas” in Quantum Communication. Simulations on this work were performed using the Finisterrae III Supercomputer, funded by the project CESGA-01 FINISTERRAE III.

AUTHOR CONTRIBUTIONS

J. D. V., M. M. J. and A. G. conceived the problem. J. D.V. developed the mathematical model and programmed the emulator. D.F. reviewed the mathematical model. All the authors contributed to analyse the data and review the manuscript.

-
- [1] S. Hochreiter and J. Schmidhuber, Long short-term memory, *Neural Computation* **9**, 1735 (1997).
 - [2] G. Zhang, B. E. Patuwo, and M. Y. Hu, Forecasting with artificial neural networks: The state of the art, *International Journal of Forecasting* **14**, 35 (1998).
 - [3] G. P. Zhang, Time series forecasting using a hybrid ARIMA and neural network model, *Neurocomputing* **50**, 159 (2003).
 - [4] K. Cho, B. van Merriënboer, C. Gulcehre, D. Bahdanau, F. Bougares, H. Schwenk, and Y. Bengio, Learning Phrase Representations using RNN Encoder–Decoder for Statistical Machine Translation, in *Proceedings of the 2014 Conference on Empirical Methods in Natural Language Processing (EMNLP)* (Association for Computational Linguistics, Doha, Qatar, 2014) pp. 1724–1734.
 - [5] G. Lai, W.-C. Chang, Y. Yang, and H. Liu, Modeling Long- and Short-Term Temporal Patterns with Deep Neural Networks, in *The 41st International ACM SIGIR Conference on Research & Development in Information Retrieval, SIGIR '18* (Association for Computing Machinery, New York, NY, USA, 2018) pp. 95–104.
 - [6] C. Zhang, D. Song, Y. Chen, X. Feng, C. Lumezanu, W. Cheng, J. Ni, B. Zong, H. Chen, and N. V. Chawla, A Deep Neural Network for Unsupervised Anomaly Detection and Diagnosis in Multivariate Time Series Data, *Proceedings of the AAAI Conference on Artificial Intelligence* **33**, 1409 (2019).
 - [7] A. Blázquez-García, A. Conde, U. Mori, and J. A. Lozano, A Review on Outlier/Anomaly Detection in Time Series Data, *ACM Comput. Surv.* **54** (2021).
 - [8] Z. C. Lipton, A Critical Review of Recurrent Neural Networks for Sequence Learning (2015), arXiv: 1506.00019.
 - [9] K. Cho, B. van Merriënboer, D. Bahdanau, and Y. Bengio, On the Properties of Neural Machine Translation: Encoder–Decoder Approaches, in *Proceedings of SSST-8, Eighth Workshop on Syntax, Semantics and Structure in Statistical Translation* (Association for Computational Linguistics, Doha, Qatar, 2014) pp. 103–111.
 - [10] A. Vaswani, N. Shazeer, N. Parmar, J. Uszkoreit, L. Jones, A. N. Gomez, L. Kaiser, and I. Polosukhin, Attention is All you Need, in *Advances in Neural Information Processing Systems*, Vol. 30 (Curran Associates, Inc., 2017).
 - [11] J. Schmidhuber, Deep learning in neural networks: An overview, *Neural Networks* **61**, 85 (2015).
 - [12] V. Dunjko and P. Wittek, A non-review of Quantum Machine Learning: trends and explorations, *Quantum Views* **4**, 32 (2020).
 - [13] J. Biamonte, P. Wittek, N. Pancotti, P. Rebentrost, N. Wiebe, and S. Lloyd, Quantum machine learning, *Nature* **549**, 195 (2017).
 - [14] M. Cerezo, A. Arrasmith, R. Babbush, S. C. Benjamin, S. Endo, K. Fujii, J. R. McClean, K. Mitarai, X. Yuan, L. Cincio, and P. J. Coles, Variational quantum algo-

- rithms, *Nature Reviews Physics* **3**, 625 (2021).
- [15] K. Mitarai, M. Negoro, M. Kitagawa, and K. Fujii, Quantum circuit learning, *Physical Review A* **98** (2018).
- [16] M. Zak and C. P. Williams, Quantum Recurrent Networks for Simulating Stochastic Processes, in *Quantum Computing and Quantum Communications*, edited by C. P. Williams (Springer Berlin Heidelberg, Berlin, Heidelberg, 1999) pp. 75–88.
- [17] L. Behera and B. Sundaram, Stochastic filtering and speech enhancement using a recurrent quantum neural network, in *International Conference on Intelligent Sensing and Information Processing, 2004. Proceedings of* (2004) pp. 165–170.
- [18] L. Behera, I. Kar, and A. C. Elitzur, A Recurrent Quantum Neural Network Model to Describe Eye Tracking of Moving Targets, *Foundations of Physics Letters* **18**, 357 (2005).
- [19] Y. Chen, F. Li, J. Wang, B. Tang, and X. Zhou, Quantum recurrent encoder–decoder neural network for performance trend prediction of rotating machinery, *Knowledge-Based Systems* **197**, 105863 (2020).
- [20] S. Y.-C. Chen, S. Yoo, and Y.-L. L. Fang, Quantum Long Short-Term Memory, in *ICASSP 2022 - 2022 IEEE International Conference on Acoustics, Speech and Signal Processing (ICASSP)* (2022) pp. 8622–8626.
- [21] A. Elkenawy, A. M. El-Nagar, M. El-Bardini, and N. M. El-Rabaie, Full-state neural network observer-based hybrid quantum diagonal recurrent neural network adaptive tracking control, *Neural Computing and Applications* **33**, 9221 (2021).
- [22] S. Y.-C. Chen, Quantum Deep Recurrent Reinforcement Learning, in *ICASSP 2023 - 2023 IEEE International Conference on Acoustics, Speech and Signal Processing (ICASSP)* (2023) pp. 1–5.
- [23] S.-T. Tsai, E. Fields, Y. Xu, E.-J. Kuo, and P. Tiwary, Path sampling of recurrent neural networks by incorporating known physics, *Nature Communications* **13**, 7231 (2022).
- [24] J. Bausch, Recurrent Quantum Neural Networks, in *Advances in Neural Information Processing Systems*, Vol. 33, edited by H. Larochelle, M. Ranzato, R. Hassel, M. F. Balcan, and H. Lin (Curran Associates, Inc., 2020) pp. 1368–1379.
- [25] Y. Takaki, K. Mitarai, M. Negoro, K. Fujii, and M. Kitagawa, Learning temporal data with a variational quantum recurrent neural network, *Physical Review A* **103** (2021).
- [26] M. Siemaszko, A. Buraczewski, B. Le Saux, and M. Stobińska, Rapid training of quantum recurrent neural networks, *Quantum Machine Intelligence* **5**, 31 (2023).
- [27] D. Bondarenko, R. Salzmann, and V.-S. Schmiesing, Learning Quantum Processes with Memory – Quantum Recurrent Neural Networks (2023), arXiv: 2301.08167.
- [28] Y. Li, Z. Wang, R. Han, S. Shi, J. Li, R. Shang, H. Zheng, G. Zhong, and Y. Gu, Quantum recurrent neural networks for sequential learning, *Neural Networks* **166**, 148 (2023).
- [29] T.-P. Sun, Z.-Y. Chen, C. Xue, S.-X. Ma, H.-Y. Liu, Y.-C. Wu, and G.-P. Guo, Quantum-Discrete-Map-Based Recurrent Neural Networks (2023), arXiv: 2305.15976.
- [30] A. D. Córcoles, M. Takita, K. Inoue, S. Lekuch, Z. K. Mineev, J. M. Chow, and J. M. Gambetta, Exploiting Dynamic Quantum Circuits in a Quantum Algorithm with Superconducting Qubits, *Physical Review Letters* **127** (2021).
- [31] IBM, Bringing the full power of dynamic circuits to Qiskit Runtime (2022), <https://research.ibm.com/blog/quantum-dynamic-circuits>.
- [32] M. Foss-Feig, A. Tikku, T.-C. Lu, K. Mayer, M. Iqbal, T. M. Gatterman, J. A. Gerber, K. Gilmore, D. Gresh, A. Hankin, N. Hewitt, C. V. Horst, M. Matheny, T. Mengle, B. Neyenhuis, H. Dreyer, D. Hayes, T. H. Hsieh, and I. H. Kim, Experimental demonstration of the advantage of adaptive quantum circuits (2023), arXiv: 2302.03029.
- [33] M. Schuld, V. Bergholm, C. Gogolin, J. Izaac, and N. Killoran, Evaluating analytic gradients on quantum hardware, *Physical Review A* **99** (2019).
- [34] A. Géron, *Hands-On Machine Learning with Scikit-Learn and TensorFlow*, 1st ed. (O’Reilly, United States, 2017).
- [35] P. Krantz, M. Kjaergaard, F. Yan, T. P. Orlando, S. Gustavsson, and W. D. Oliver, A quantum engineer’s guide to superconducting qubits, *Applied Physics Reviews* **6**, 021318 (2019).
- [36] J. L. Elman, Finding Structure in Time, *Cognitive Science* **14**, 179 (1990).
- [37] A. G. Baydin, B. A. Pearlmutter, A. A. Radul, and J. M. Siskind, Automatic Differentiation in Machine Learning: A Survey, *The Journal of Machine Learning Research* **18**, 5595 (2017).
- [38] P. Werbos, Backpropagation through time: what it does and how to do it, *Proceedings of the IEEE* **78**, 1550 (1990).
- [39] H. Jaeger, Tutorial on training recurrent neural networks, covering BPPT, RTRL, EKF and the echo state network approach, *GMD-Forschungszentrum Informationstechnik* **5** (2002).
- [40] A. Zhang, Z. C. Lipton, M. Li, and A. J. Smola, Dive into Deep Learning (2023), arXiv: 2106.11342.
- [41] C. Tallec and Y. Ollivier, Unbiasing Truncated Backpropagation Through Time (2017), arXiv: 1705.08209.
- [42] A. W. Harrow and J. C. Napp, Low-Depth Gradient Measurements Can Improve Convergence in Variational Hybrid Quantum-Classical Algorithms, *Physical Review Letters* **126** (2021).
- [43] D. Wierichs, J. Izaac, C. Wang, and C. Y.-Y. Lin, General parameter-shift rules for quantum gradients, *Quantum* **6**, 677 (2022).
- [44] M. Benedetti, E. Lloyd, S. Sack, and M. Fiorentini, Parameterized quantum circuits as machine learning models, *Quantum Science and Technology* **4**, 043001 (2019).
- [45] S. Wisdom, T. Powers, J. Hershey, J. Le Roux, and L. Atlas, Full-Capacity Unitary Recurrent Neural Networks, in *Advances in Neural Information Processing Systems*, Vol. 29, edited by D. Lee, M. Sugiyama, U. Luxburg, I. Guyon, and R. Garnett (Curran Associates, Inc., 2016).
- [46] J. R. McClean, S. Boixo, V. N. Smelyanskiy, R. Babush, and H. Neven, Barren plateaus in quantum neural network training landscapes, *Nature Communications* **9**, 4812 (2018).
- [47] M. Cerezo, A. Sone, T. Volkoff, L. Cincio, and P. J. Coles, Cost function dependent barren plateaus in shallow parametrized quantum circuits, *Nature Communications* **12** (2021).
- [48] P. Huembeli and A. Dauphin, Characterizing the loss landscape of variational quantum circuits, *Quantum Science and Technology* **6**, 025011 (2021).

- [49] K. Mitarai and K. Fujii, Methodology for replacing indirect measurements with direct measurements, *Physical Review Research* **1** (2019).
- [50] M. Schuld, R. Sweke, and J. J. Meyer, Effect of data encoding on the expressive power of variational quantum-machine-learning models, *Physical Review A* **103** (2021).
- [51] A. Pérez-Salinas, A. Cervera-Liarta, E. Gil-Fuster, and J. I. Latorre, Data re-uploading for a universal quantum classifier, *Quantum* **4**, 226 (2020).
- [52] B. Casas and A. Cervera-Liarta, Multidimensional Fourier series with quantum circuits, *Phys. Rev. A* **107**, 062612 (2023).
- [53] C. Zhu, R. H. Byrd, P. Lu, and J. Nocedal, Algorithm 778: L-BFGS-B: Fortran Subroutines for Large-Scale Bound-Constrained Optimization, *ACM Transactions on Mathematical Software* **23**, 550 (1997).
- [54] P. Virtanen, R. Gommers, T. E. Oliphant, M. Haberland, T. Reddy, D. Cournapeau, E. Burovski, P. Peterson, W. Weckesser, J. Bright, S. J. van der Walt, M. Brett, J. Wilson, K. J. Millman, N. Mayorov, *et al.*, SciPy 1.0: fundamental algorithms for scientific computing in Python, *Nature Methods* **17**, 261 (2020).

Appendix A: A further explanation on tensor notation

In this paper, the mathematical formulation contains 0-to-5-rank tensors. A main character plus a set of indices identify the tensors. This notation is valuable (i) to have more compact formulas by decreasing the bra-ket notation and (ii) to show the expression to implement in a classical emulation code.

5-rank tensors are represented by an upper shift letter that contains a lower index in parenthesis, indicating the time step (circuit block number). Let \mathcal{H}_E and \mathcal{H}_M be the Hilbert spaces corresponding to registers E and M, respectively. The equivalence for a quantum operator in terms of projectors is

$$U_{(t)kl}^{ij} = a |i \otimes j\rangle \langle k \otimes l|, |i\rangle \in \mathcal{H}_E, \langle k| \in \mathcal{H}_E^*, |j\rangle \in \mathcal{H}_M, \langle l| \in \mathcal{H}_M^*, \quad (\text{A1})$$

where a is actually a scalar, the numerical value of the corresponding component. A density matrix is represented with the same form.

4-rank tensors are equivalent to 5-rank ones, but omitting the time label (t). 3-rank tensors could appear in different forms, depending on the indices positioning.

2-rank tensors also depend on the index positioning. A lowercase letter with two indices above represents a quantum state living in the $\mathcal{H}_E \otimes \mathcal{H}_M$ space, which in terms of state vectors is

$$v^{ij} = a |i \otimes j\rangle, |i\rangle \in \mathcal{H}_E, |j\rangle \in \mathcal{H}_M, \quad (\text{A2})$$

while its Hermitian conjugate is

$$v_{ij} = a \langle i \otimes j|, \langle i| \in \mathcal{H}_E^*, \langle j| \in \mathcal{H}_M^*. \quad (\text{A3})$$

A symbol with one index up and one down represents an operator or a density matrix living in one of the Hilbert spaces,

$$U_k^i = a |i\rangle \langle k|, |i\rangle \in \mathcal{H}_R, \langle k| \in \mathcal{H}_R^*, R \in \{E, M\}. \quad (\text{A4})$$

1-rank tensors are actually (state)vectors living in only one of the (dual) Hilbert spaces,

$$v^i = a |i\rangle \text{ or } w_i = b \langle i|, |i\rangle \in \mathcal{H}_R, \langle i| \in \mathcal{H}_R^*, R \in \{E, M\}. \quad (\text{A5})$$

0-rank tensors are represented by a symbol without any indices, and they are scalars.

We show the equivalences of operations in Eq. (A6). Indices can appear as single values or pairs, depending on whether the corresponding Hilbert space is $\mathcal{H} \in \{\mathcal{H}_E, \mathcal{H}_M\}$ or $\mathcal{H}_E \otimes \mathcal{H}_M$.

(unitary operation)	$(U v\rangle)^i$	=	$U_k^i v^k$	(A6)
(unitary product)	$(U \cdot V)_k^i$	=	$U_m^i V_k^m$	
(vectors tensor product)	$(v\rangle \otimes w\rangle)^{ij}$	=	$v^i w^j$	
(vectors outer product)	$(v\rangle \langle w)_j^i$	=	$v^i w_j^*$	
(matrix tensor product)	$(U \otimes V)_{kl}^{ij}$	=	$U_k^i V_l^j$	
(hermitian conjugate)	$(U^\dagger)_k^i$	=	U_i^{k*}	
(trace)	$\text{Tr } \rho$	=	$\rho_{jl}^{ik} \delta_{ik}^{jl}$	
(partial trace A)	$(\text{Tr}_A \rho)_l^k$	=	$\rho_{il}^{ik} = \rho_{jl}^{ik} \delta_i^j$	
(partial trace B)	$(\text{Tr}_B \rho)_j^i$	=	$\rho_{jk}^{ik} = \rho_{jl}^{ik} \delta_k^l$	

Note that the tensor product operation does not commute, therefore, the writing order does affect the final result. We use the Einstein summation convention where indices that appear twice (up and down) in a term imply the summation of that term over all the values of the index. The symbol δ is the Kronecker delta and allows to raise and lower indices, as shown in partial trace operations. In order to avoid ambiguities or to highlight the operation, operators, quantum states, and density matrices are defined in the text and explicit summation operators are shown when necessary.

In Section II C, summation runs over N_E for indices identifying register E (first index of a pair or index of the first element in a tensor product) and N_M for indices identifying register M (second index or index of the second element).

In the case of Jacobian (gradient) and Hessian elements (Section III), they can be also thought of as tensors, and the convention is: upper indices for rows, lower indices for columns; first index of a pair for circuit block and second index of a pair for the parameter number.

Appendix B: Derivation of the Parameter Shift Rule for a QRNN circuit

Analytical partial derivatives of expectation values from circuits based on parameterised rotations are computed as [25]

$$\partial_i \langle O \rangle = \partial_i \text{Tr} [U \rho_{(t)} U^\dagger O] = \text{Tr} [\partial_i U \rho_{(t)} U^\dagger O] + \text{Tr} [U \rho_{(t)} \partial_i U^\dagger O] + \text{Tr} [U \partial_i \rho_{(t)} U^\dagger O], \quad (\text{B1})$$

where the first two terms can be computed with the well-known PSR, by shifting the parameter θ_i at circuit block t ,

$$\begin{aligned} & \text{Tr} [\partial_i U \rho_{(t)} U^\dagger O] + \text{Tr} [U \rho_{(t)} \partial_i U^\dagger O] = \\ & \frac{1}{2} \left\{ \text{Tr} \left[\partial_i U \left(\theta_i + \frac{\pi}{2} \right) \rho_{(t)} U^\dagger \left(\theta_i + \frac{\pi}{2} \right) O \right] - \text{Tr} \left[\partial_i U \left(\theta_i - \frac{\pi}{2} \right) \rho_{(t)} U^\dagger \left(\theta_i - \frac{\pi}{2} \right) O \right] \right\}, \end{aligned} \quad (\text{B2})$$

as in [15, 33]. For the latter term,

$$\text{Tr} [U \partial_i \rho_{(t)} U^\dagger O] = \text{Tr} [U \partial_i (\rho_0 \otimes \rho_{M(t-1)}) U^\dagger O] = \text{Tr} [U (\rho_0 \otimes \text{Tr}_E [\partial_i (U \rho_{(t-1)} U^\dagger)]) U^\dagger O], \quad (\text{B3})$$

where $\rho_0 = (|0\rangle\langle 0|)^{\otimes n_E}$. By applying the chain rule, we get again three terms,

$$\partial_i (U \rho_{(t-1)} U^\dagger) = \partial_i U \rho_{(t-1)} U^\dagger + U \rho_{(t-1)} \partial_i U^\dagger + U \partial_i \rho_{(t-1)} U^\dagger. \quad (\text{B4})$$

The contribution from the first two is calculated by shifting the parameter θ_i twice at block $t-1$, as in Eq. (B2), while the third one depends on $t-2$ block. Then, the equation is recursive. Each block at $t_k < t$ contributes summing with two terms corresponding to the shifts $+\pi/2$ and $-\pi/2$. The recursion ends at $t_k = 0$, then

$$\partial_i \langle O \rangle_{(t)} = \sum_{r=0}^t \frac{1}{2} \left(\langle O \rangle_{(t)}^+ \Big|_{r_i} - \langle O \rangle_{(t)}^- \Big|_{r_i} \right), \quad (\text{B5})$$

where $\langle O \rangle_{(t)}^\chi \Big|_{r_i}$ is the expectation value at time t after a χ -shift of the parameter θ_i at time t_k , with $\chi \in \{+\pi/2, -\pi/2\}$. The shift is represented uniquely by the sign for simplicity. This is the equation in the main text, where we have indicated all the shifts positioning only after the brackets.

For the Hessian, we take every term from Eq. (B5), $\langle O \rangle_{(t)}^\chi \Big|_{r_i}$, and apply again the PSR,

$$\partial_j \langle O \rangle_{(t)}^\chi \Big|_{r_i} = \text{Tr} (\partial_j U' \rho_{(t)} U'^\dagger O)^\chi \Big|_{r_i} + \text{Tr} (U' \rho_{(t)} \partial_j U'^\dagger O)^\chi \Big|_{r_i} + \text{Tr} (U' \partial_j \rho_{(t)} U'^\dagger O)^\chi \Big|_{r_i}, \quad (\text{B6})$$

being $U' = U(\theta_i + \chi)$. The subsequent derivation is now analogue to the one for the first-order PSR. From Eq.(B5), now

$$\partial_i \partial_j \langle O \rangle_{(t)} = \frac{1}{4} \sum_r^t \sum_s^t \left(\langle O \rangle_{(t)}^{++} \Big|_{s_j}^{r_i} + \langle O \rangle_{(t)}^{--} \Big|_{s_j}^{r_i} - \langle O \rangle_{(t)}^{+-} \Big|_{s_j}^{r_i} - \langle O \rangle_{(t)}^{-+} \Big|_{s_j}^{r_i} \right), \quad (\text{B7})$$

where $\langle O \rangle_{(t)}^{\chi\lambda} \Big|_{s_j}^{r_i}$ is the expectation value at time t after a shift χ in the parameter θ_i at block r and a shift λ in the parameter θ_j at block s . Then, we have 4 different circuits per term in sums. For the case $i = j$, $\langle O \rangle_{(t)}^{\chi\lambda} \Big|_{s_j}^{r_i}$ is invariant under $r \leftrightarrow s$ exchange, then, we do not need to expand the full sum over s in Eq. (B7), but only up to r . Moreover, when $i = j$ and $r = s$, equal-sign shifts become a single π -shift and contrary-sign shifts cancel. Then,

$$\begin{aligned} \partial_i^2 \langle O \rangle_{(t)} &= \frac{1}{2} \sum_r^t \sum_s^{r-1} \left(\langle O \rangle_{(t)}^{++} \Big|_{s_i}^{r_i} + \langle O \rangle_{(t)}^{--} \Big|_{s_i}^{r_i} \right) + \frac{1}{2} \sum_r^t \left(\langle O \rangle_{(t)}^{++} \Big|_{r_i}^{r_i} + \langle O \rangle_{(t)}^{--} \Big|_{r_i}^{r_i} \right) - \\ & \quad - \frac{1}{2} \sum_r^t \sum_s^{r-1} \left(\langle O \rangle_{(t)}^{+-} \Big|_{s_i}^{r_i} + \langle O \rangle_{(t)}^{-+} \Big|_{s_i}^{r_i} \right) - \frac{1}{2} \sum_r^t \langle O \rangle_{(t)}^{r_i}, \end{aligned} \quad (\text{B8})$$

which is equivalent to the equation in the main text. Since all the possible combinations of r and s are computed, the Hessian is symmetric under $i \leftrightarrow j$ exchange.

The number of different circuits to execute, needed to compute the Hessian of the T observables $\langle O \rangle_{(t)}$ with t from 0 to $T - 1$, is then

$$4 \times \frac{N_\theta(N_\theta - 1)}{2} T^2 + 2 \times N_\theta \frac{T(T + 1)}{2} + 2 \times N_\theta \frac{T(T - 1)}{2} + 1 = 2N_\theta^2 T^2 + 1. \quad (\text{B9})$$

Appendix C: Machine Learning task details

We have accomplished the machine learning of the three datasets by a classical machine emulating the ideal PQC by an algorithm based on the formulas derived in Section II. The optimiser is L-BFGS-B, a gradient-based minimiser [53]. The emulation has been simply performed by matrix calculations with *NumPy*, leveraging the reductions in operations provided by the formulation. We employed the L-BFGS-B method in `scipy.optimize.minimize`, from the open-source library *SciPy* [54], as the optimisation algorithm. The `multiprocessing` package was used to parallelise the analytical gradient components.

The optimiser starts at a randomly generated point in the parameter landscape (except the bias b , which is initialised to 0), and we execute 8 different optimisations with different random initialisations. Convergence criteria are $g_{\text{tol}} = 10^{-3}$ for case (a) and $g_{\text{tol}} = 10^{-4}$ for cases (b) and (c), being g_{tol} the threshold for the maximum component of the projected gradient. Maximum number of iterations is set to 1000. Optimisations that achieve a worse validation RMSE are discarded, and only the best one was selected as the solution, which is the one plotted. The worst results than the selected ones are due to vanishing gradients through the optimisation process. However, the predictions always tend to converge to solutions near the expected ones (relative RMSE $\lesssim 0.1$).

The three different datasets were generated as explained in the following paragraphs.

Case (a) is a triangular dimmed signal described by the equation

$$s(t) = A e^{-\mu t} g(P, t), \quad (\text{C1})$$

where $g(P, t)$ is a triangular signal of period P . Input series is directly got from this equation, while the reference output series is the same series several steps forward in time, i.e.,

$$y(t) = s(t + t_d). \quad (\text{C2})$$

Case (b) is a forced Van der Pol signal, described by the differential equation

$$\frac{ds^2}{dt^2} - \mu(1 - s^2) \frac{ds}{dt} + s = A \sin(\omega t), \quad (\text{C3})$$

where the right-hand side is a sinusoidal perturbation. The input series is

$$x(t) = c s(t), \quad (\text{C4})$$

while the label is

$$y(t) = c s(t + t_d). \quad (\text{C5})$$

Case (c) consists of two Van der Pol signals without perturbation, each of them described by the equation

$$\frac{ds_i^2}{dt^2} - \mu_i(1 - s_i^2) \frac{ds_i}{dt} + s_i = 0. \quad (\text{C6})$$

The input series are given by

$$x_i(t) = c_i s_i(t), \quad (\text{C7})$$

while the label series is

$$y(t) = d_0 x_0(t + t_0) + d_1 x_1(t + t_1). \quad (\text{C8})$$

All the series are 1000 points, filling times from $t = 0$ to 100. Note that in this Appendix, the value t represents the physical time, but not the time step (point) in the time series. The parameters of the dataset generators are summarised in Eq. (C9).

$$\begin{aligned} \text{(a)} \quad & A = 0.75 \quad \mu = 0.02 \quad T = 5 \quad t_d = 12 \\ \text{(b)} \quad & A = 1 \quad c = 0.25 \quad \mu = 2 \quad \omega = 5 \quad t_d = 15 \\ \text{(c)} \quad & c_0 = 0.25 \quad d_0 = 1 \quad \mu_0 = 2 \quad t_0 = 5 \quad c_1 = 0.25 \quad d_1 = 0.1 \quad \mu_1 = 1 \quad t_1 = 18 \end{aligned} \tag{C9}$$